Improved model of rectangular scratch drive actuator

Shawn Chen
Chiawei Chang
Wensyang Hsu
National Chiao Tung University
Department of Mechanical Engineering
1001 University Road
Hsinchu 300, Taiwan
E-mail: whsu@mail.nctu.edu.tw

Abstract. This paper proposes an integrated model of a scratch drive actuator (SDA) based on a fourth-order governing equation of the Euler–Bernoulli theory. By solving this equation with proper boundary conditions, typical SDA output characteristics, such as noncontact length, priming voltage, deflection curve, output force, and bending stress, can be determined. The results of the output force in a static model are then used as the input of single degree-of-freedom dynamic SDA model to investigate the friction effect. Electroplated nickel SDA arrays, 80 μm in main beam length and 65 μm in width with a suspended spring, are fabricated and tested. The average travel distances after 1500 input pulses of 80–120 V are measured and found to be from 4.7 to 12.9 μm. The average measured output forces are from 10.2 to 28.3 μN. The simulation from the dynamic model is closer to the measured total travel distance and the output force than the static model, in general. The difference between simulations and experimental data due to energy dissipation can be reduced by including the friction effect in the dynamic model. Deviations between simulations and measured results are less than 10% in full range showing the superior capability of the proposed SDA model. [DOI: 10.1117/1.3549920]

Subject terms: scratch drive actuator; friction effects; dynamic modeling; static deflection; vibration induced motion; MEMS.

Paper 10070R received Jun. 18, 2010; revised manuscript received Dec. 12, 2010; accepted for publication Jan. 3, 2011; published online Mar. 25, 2011; corrected Apr. 4, 2011.

1 Introduction

Most electrostatic microactuators operate in a linear region before pull-in occurs. One major exception is the scratch drive actuator (SDA), which is nonlinearly operated in a postpriming region.[1] The unique features of the SDA include force output in micro-Newton order, stepping ahead at nanometer resolution, and long traveling ability up to the millimeter level. These features make it attractive in micro- and nanomanipulation.[2–6] However, most present models are basically piecewise in analyzing SDA performance and limited in the static region due to the complexity of the nonlinearly dynamic coupling between electrostatic, mechanical, and friction forces. Despite its importance in the field of MEMS, the SDA is not well understood.

Some researchers have attempted to explore the relationship between the step size and the input voltage of the SDA. The step size under constant load is the most fundamental case and has been studied by using various methods. One approach was to measure the contact length of a charged SDA with an insulated layer by using an interference image, and then to calculate the step size from the geometry of selected images.[1,2] This approach did not analytically relate the step size and input voltage. Another approach used a second-order differential equation[5] to predict the step size by using a modified Petersen model. As the moment and deflection equations are from different assumptions, the prediction of priming was higher than the experimental data. An energy method was used by treating the reaction force at bushing as a concentrated load.[7] Since electrostatic force did distribute along the main beam during operation, the predicted step size was overestimated in comparison with measured results.[7,8] For the step size with a variable load, such as an SDA connected to a suspended spring under a continuous loading and unloading process, it was usually experimentally determined by averaging the measured total forward distance with the total input pulses.[5,9] However, it must be pointed out that the spring force proportional to the deflection dynamically affects the step size. The step size becomes zero when the spring force is equal to the output force of the SDA. For the determination of the SDA output force, only experimental approaches have been reported, including buckled-load[2] and spring-deflection[5,9] methods. Until now, no analytical formulation has been reported to demonstrate the dynamic behaviors of the SDA, including the variable loading and the friction effects.

One way to simulate the dynamic response of the SDA to cyclic input is to treat it as a mass-spring-damper system of a single degree of freedom (SDOF) under cyclic input of an electrostatic force, which can be classified as vibration-induced motion.[10,11] By integrating the equations of motion, the displacement and the velocity of the mass can be numerically found.

Two analytical models of the SDA are proposed here to analyze the static and dynamic behaviors in sequence. First, a fourth-order differential governing equation based on the Euler–Bernoulli theory and the modified Petersen model with a distributed electrostatic force is proposed. The performance and characteristics of the SDA, such as the deflection curve of the main beam, the static step size, the bending moment, the maximum stress, and the output force at a given input voltage, could all be determined for the first time in SDA analysis. Second, an SDOF model of an SDA is proposed to analyze

1932-5150/2011/$25.00 © 2011 SPIE

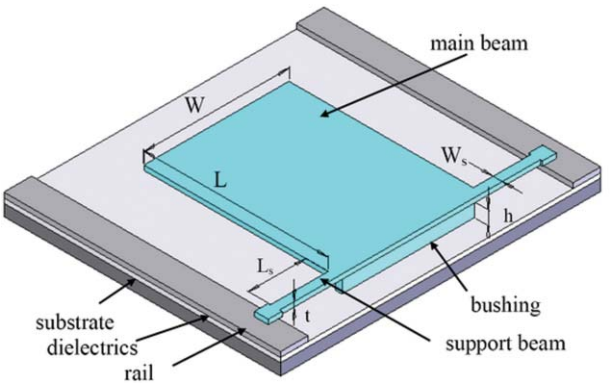

Fig. 1 Basic structure and elements of the SDA.

the vibrational motion to find the total travel distance and the dynamic output force under various sets of friction conditions and spring constants. In order to verify the proposed models, the microelectroplated nickel SDA array connected with a suspended spring is fabricated and tested to compare with simulation results.

2 Modeling of SDA

2.1 *Operation Principle of SDA*

A typical SDA may include the main beam, bushing, support beams, rails, dielectrics, and a substrate, as shown in Fig. 1. The operation of an SDA from rest to scratch forward is classified into five states, as shown in Fig. 2: (1) initial, (2) pull in, (c) priming, (d) postpriming, and (e) one-step forward after discharge. As the input voltage V increases from zero, the still SDA [Fig. 2(a)] starts rotating about the bushing paw and the end edge of the main beam will just touch the dielectrics at the pull-in voltage, V_{pi} [Fig. 2(b)]. For input voltage higher than pull-in voltage V_{pi}, the main beam

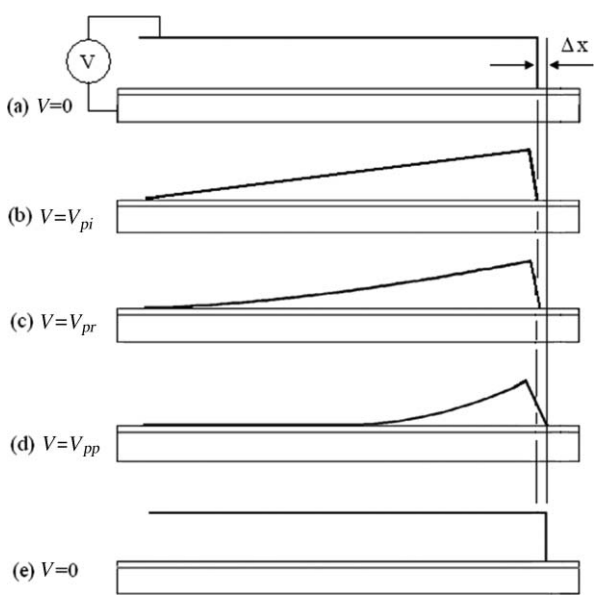

Fig. 2 Five states in SDA operation procedures at different input voltages: (a) initial, zero input; (b) pull-in, voltage V_{pi}; (c) priming, voltage V_{pr}; (d) postpriming, voltage V_{pp}; (e) one-step forward after discharge.

will be bent and gradually becomes a surface contact with the dielectrics [Fig. 2(c)], so-called priming, at input voltage V_{pr}. In priming state, the contact point between the bushing paw and the dielectrics may be pushed forward a little. After that, the contact length of the main beam with dielectrics increases as the input voltage increases in postpriming range at voltage V_{pp}, as shown in Fig. 2(d). The contact point between the bushing paw and the dielectrics will be pushed forward more to achieve one forward step. Finally, the input voltage is fully discharged, and the SDA will snap back and keep the one forward step, as shown in Fig. 2(e).

2.2 *Static Analysis of SDA Deflection*

Some assumptions are made first. The Euler–Bernoulli theory is applied to the design and analysis of the main and the support beams. The bushing, dielectrics, and rails are assumed rigid. The angle between the bushing and the main beam remains as a right angle during the whole operation, and the electrostatic force acted upon the bushing is ignored. At the pull-in, priming, and postpriming states, the contact between the main beam and the dielectrics remains fixed. In other words, one end of the main beam is fixed and only the bushing can move at the priming and the postpriming states. No slippage occurs during charging and discharging. The vertical displacement of the bushing top is negligible during main beam deflection in the priming and the postpriming states. The fringing effect of the electrostatic field is ignored.

For a general parallel-plate capacitor, the distributed load q, i.e., the electrostatic force per unit length applied to the plate, is given as a constant

$$q = \frac{\varepsilon_0 W V^2}{2d^2}, \tag{1}$$

where ε_0 is the permittivity of air, V is the input voltage, W is the width of the plate, and d is the gap between two plates. Let the SDA be modeled as a plate capacitor, d is defined as the distance from the main beam to the electrode on the substrate, including air and the dielectric layers. The distance d will be varied with the main beam deflection y by electrostatic load q and constrained by the bushing and support beams, where q should be a function of the horizontal position x and the main beam deflection y. Due to this nonlinear coupling between the electrostatic load q and the main beam deflection y, there is not yet an exact solution for the deflection curve y thus far. A modified Petersen model has been proposed to define the deflection curve of a cantilever beam under an electrostatic force as a second-order polynomial of horizontal position x in a postpriming state.[5] By combining the Euler–Bernoulli beam theory[12] and the modified Petersen model,[5,13] the governing equation of the main beam with the distributed electrostatic load $q(x)$ at a postpriming state can be expressed as a fourth-order differential equation:

$$\frac{\mathrm{d}^4 y}{\mathrm{d}x^4} = \frac{q(x)}{EI} = \frac{\varepsilon_0 W V^2}{EI(a+bx^2)^2}, \tag{2}$$

where a is equal to the thickness t of the dielectric layer divided by the relative permittivity k, b is equal to h / l_n^2, l_n is the noncontact length of the main beam at the given input voltage, h is the bushing height, E is Young's modulus of the SDA material, I is the second-area moment of the main beam, and x is the horizontal coordinate of the element in consid-

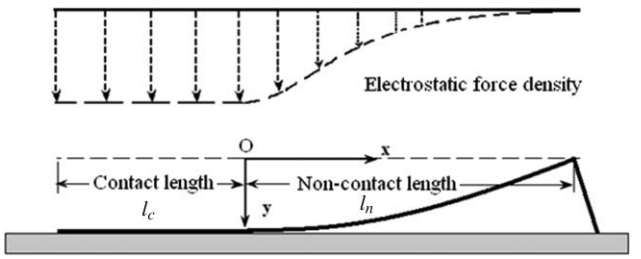

Fig. 3 Coordinate system and electrostatic force density in postpriming configuration. The electrostatic force density in the contact region is constant. In the noncontact region, the electrostatic force density follows Eq. (2).

eration. The downward deflection is defined as positive. The coordinate system is shown in Fig. 3, where the origin is defined as the juncture point between the contact and noncontact regimes with distance h above. Integrating Eq. (2) successively four times leads to the following equations:

$$\frac{d^3y}{dx^3}=\frac{\varepsilon_0 WV^2}{EI}\left[\frac{x}{2a(a+bx^2)}+\frac{\tan^{-1}[bx/(ab)^{1/2}]}{2a(ab)^{1/2}}\right]+c_1, \quad (3)$$

$$\frac{d^2y}{dx^2}=\frac{\varepsilon_0 WV^2}{EI}\left[\frac{\ln a}{4ab}+\frac{x\tan^{-1}[bx/(ab)^{1/2}]}{2a(ab)^{1/2}}\right]+c_1x+c_2, \quad (4)$$

$$\frac{dy}{dx}=\frac{\varepsilon_0 WV^2}{EI}\left[\frac{x(\ln a-1)}{4ab}+\frac{(a+bx^2)\tan^{-1}[bx/(ab)^{1/2}]}{4(ab)^{3/2}}\right]+\frac{c_1}{2}x^2+c_2x+c_3, \quad (5)$$

$$y=\frac{\varepsilon_0 WV^2}{EI}\left[\frac{3\ln a-2\ln\left(1+bx^2/a\right)}{24b^2}+\frac{3x^2\ln a-4x^2}{24ab}+\frac{(3ax+bx^3)\tan^{-1}[bx/(ab)^{1/2}]}{12(ab)^{3/2}}\right]+\frac{c_1}{6}x^3+\frac{c_2}{2}x^2+c_3x+c_4. \quad (6)$$

The integration constants, c_1, c_2, c_3, c_4, and noncontact length l_n, can be solved with the following five boundary conditions:

$$y(0)=h, \quad (7)$$

$$y'(0)=0, \quad (8)$$

$$y''(0)=0, \quad (9)$$

$$y(l_n)=0, \quad (10)$$

$$k_t y'(l_n)=EIy'(l_n). \quad (11)$$

The y coordinate of the contact point is the bushing height h, as indicated by Eq. (7). Also, the contact region is flat and fixed to the dielectrics at a postpriming state, so the slope and moment at origin O are zero, as implied by Eqs. (8) and (9), respectively. Equation (10) states that the vertical displacement of the bushing is negligible. Equation (11) expresses the balance between the moment $EIy''(l_n)$ of the main beam and the torque $k_{t\,y'}(l_n)$ from the support beam at $x=l_n$. The parameter k_t is the torsional spring constant of the support beam and is defined as $2\beta GW_s t^3/L_s$, where β is a constant based on the ratio of the width to thickness of the support beam,[14] W_s is the width of the support beam, L_s is the length of the support beam, and G is the shear modulus of the SDA material.

Applying the boundary conditions Eqs. (7)–(9) into characteristic Eqs. (4)–(6), the integration constants c_2, c_3, and c_4 can be solved as

$$c_2=-\frac{\varepsilon_0 WV^2}{EI}\frac{\ln a}{4ab}, \quad (12)$$

$$c_3=0, \quad (13)$$

$$c_4=h-\frac{\varepsilon_0 WV^2}{EI}\left(\frac{l_n^4\ln a}{8h^2}\right). \quad (14)$$

Applying Eq. (10) into characteristic Eq. (3), the integration constant c_1 can be solved as

$$c_1=\frac{\varepsilon_0 WV^2}{EI}\left[\frac{1}{abl_n}-\frac{\left(3a+bl_n^2\right)\tan^{-1}[bl_n/(ab)^{1/2}]}{2(ab)^{3/2}l_n^2}+\frac{\ln(1+bl_n^2/a)}{2b^2l_n^3}\right]-\frac{6h}{l_n^3}. \quad (15)$$

Rewriting the expression of Eq. (11) in terms of Eqs. (4) and (5) can lead to the characteristic equation of noncontact length l_n

$$k_t\left\{\frac{\varepsilon_0 WV^2}{EI}\left[\frac{-2a\tan^{-1}[bl_n/(ab)^{1/2}]}{4(ab)^{3/2}}+\frac{\ln(1+bl_n^2/a)}{4b^2l_n}+\frac{l_n}{4ab}\right]-\frac{3h}{l_n}\right\}=\left\{\varepsilon_0 WV^2\left[-\frac{3a\tan^{-1}[bl_n/(ab)^{1/2}]}{2(ab)^{3/2}l_n}+\frac{1}{ab}+\frac{\ln(1+bl_n^2/a)}{2b^2l_n^2}\right]-\frac{6EIh}{l_n^2}\right\}. \quad (16)$$

Since no explicit solution exists, the noncontact length l_n is solved by a numerical method. At the priming state, the noncontact length is considered to be the same as the main beam length L. Then, the priming voltage V_{pr} can be determined from reorganizing Eq. (16) by replacing l_n with the main beam length L as

$$V_{pr} = \left[\frac{(3k_t h/L - 6EIh/L^2)}{A_1 - A_2}\right]^{1/2}, \tag{17}$$

where

$$A_1 = \frac{\varepsilon_0 k_t W}{EI}\left[\frac{-2a\tan^{-1}[bL/(ab)^{1/2}]}{4(ab)^{3/2}} + \frac{\ln(1+bL^2/a)}{4bL} + \frac{L}{4ab}\right], \tag{18}$$

$$A_2 = \varepsilon_0 W\left[-\frac{3a\tan^{-1}[bL/(ab)^{1/2}]}{2(ab)^{3/2}L} + \frac{1}{ab} + \frac{\ln(1+bL^2/a)}{2b^2L^2}\right]. \tag{19}$$

By definition, the bending moment M at any position x along the main beam is proportional to the second-order derivative of y. When flexural rigidity EI is constant, the bending moment can be expressed as

$$M = -EI\frac{d^2y}{dx^2} = \varepsilon_0 W V^2\left(\frac{bl_n^2 x\left(-\tan^{-1}[bx/(ab)^{1/2}] + \tan^{-1}[bl_n/(ab)^{1/2}]\right) + 3ax\tan^{-1}[bl_n/(ab)^{1/2}]}{2(ab_2)^{3/2}l_n^2} - \frac{x}{abl_n} - \frac{x\ln[1+bl_n^2/a]}{2b^2l_n^3}\right) + \frac{6EIh}{l_n^3}x. \tag{20}$$

The maximum moment M_m along the main beam for a specific input voltage occurs at position x_m where the shear force, $-EI\,dy/dx$, becomes zero. Then, the maximum bending stress σ_m along the main beam happens at the same position and can be expressed as

$$\sigma_m = \frac{6M_m}{Wt^2}. \tag{21}$$

The output force F_o of a charged SDA array along the main beam varies with the input voltage. The friction force along the contact regime is assumed to be large enough to keep the contact area stationary. The horizontal output force F_o is basically the horizontal component of the electrostatic force along the main beam. It can be solved by integrating the horizontal component of electrostatic force along the noncontact part as

$$F_o = N\int_0^{ln}\frac{\varepsilon_0 W V^2\sin\theta}{(a+bx^2)^2}dx, \tag{22}$$

where N is the SDA number in the SDA array and θ is the angle between the horizontal and the tangent line along the main beam.

In finding the static step size, Fig. 4 shows the displacements of the bushing paw and the bushing top at different input voltages. At pull-in voltage, the SDA rotates about the bushing paw. Due to the slope change on the bushing, the bushing top horizontally moves back with magnitude $\Delta x_1 = h^*\tan^{-1}(h/L)$, as shown in Fig. 4(a). When the input voltage exceeds the priming voltage, the main beam starts bending and causes the bushing top to move further backward due to the bending moment, the so-called curvature shortening effect, which has not been considered in previous literature on the SDA. This lateral displacement due to a curvature shortening effect[12] can be formulated as $\Delta x_2 = 1/2\int_0^{ln}(dy/dx)^2dx$, as shown in Fig. 4(b). Since the angle between the main beam and the rigid bushing is assumed to remain 90 deg during deformation, the bushing paw has to move forward. Then, the horizontal distance between the bushing top and the bushing paw becomes $\Delta x_3 = h^*|dy/dx|$ [Fig. 4(c)]. By combining these three effects, the net one forward step size of the bushing paw in static load becomes [Fig. 4(d)]

$$\Delta x_s = \Delta x_3 - \Delta x_1 - \Delta x_2 = h*\left(\left|\frac{dy}{dx}\right|_{x=L} - \tan^{-1}\frac{h}{L}\right) - \frac{1}{2}\int_0^{ln}\left(\frac{dy}{dx}\right)^2 dx. \tag{23}$$

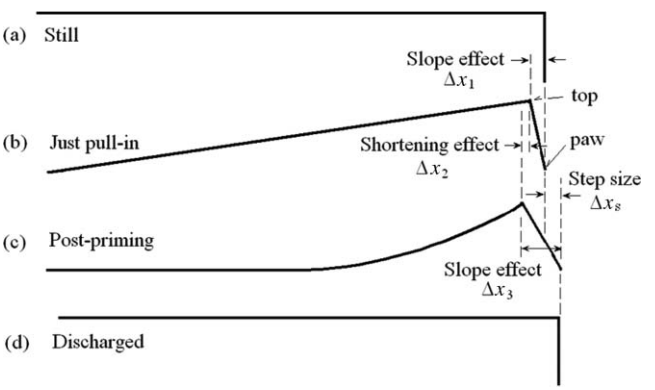

Fig. 4 Components of the SDA step size. (a) Initial state without movement. (b) The main beam rotates around the bushing paw when just the pull in can cause lateral backward movement Δx_1. (c) The curvature shortening effect in a postpriming regime causes the bushing top lateral movement Δx_2 further backward. Also, the bushing paw displaces Δx_3 forward and keeps 90 deg with the main beam. (d) The SDA is discharged fully with one net step size $\Delta x_s = \Delta x_3 - \Delta x_1 - \Delta x_2$.

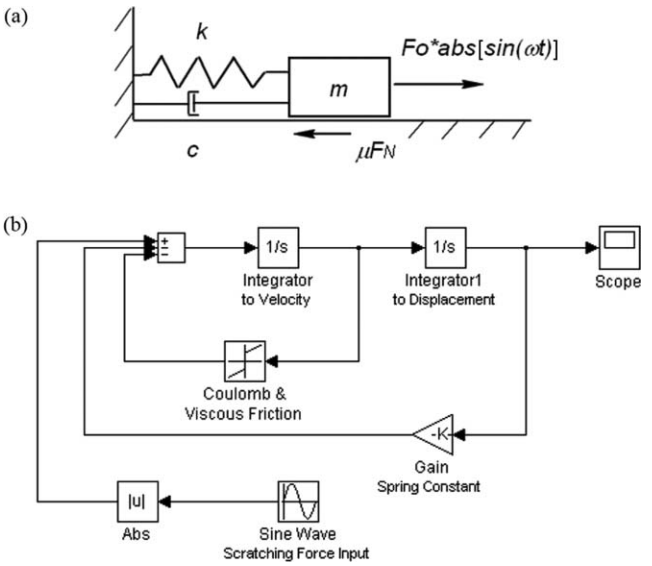

Fig. 5 Dynamic model of the SDA. (a) SDOF Mass-spring-damper model. (b) Simulink model of the SDA system.

Two different equations are proposed here to calculate the static step size in each input pulse and the total travel distance of the SDA array with a restoring spring force after certain input pulses:

$$\Delta x(n) = \Delta x_0^*[F_o - k^* x(n-1)]/F_o, \tag{24}$$

$$x(n) = x(n-1) + \Delta x(n), \tag{25}$$

where the $\Delta x(n)$ is the step size at the n'th input pulse and Δx_0 is the step size without considering external load, calculated from Eq. (23). The $x(n)$ is the total travel distance of the SDA array after n input pulses, k is the spring constant, and F_0 is the output force of the SDA array calculated from Eq. (22). The $x(0)$ is set to zero. Qualitatively speaking, the restoring force of the spring is small at the beginning of the test and the step size is close to the calculated value without the external load. As the spring deflection increases, the step size decreases with the increasing spring load. When the SDA array can no longer pull the spring, the step size becomes zero.

2.3 *Dynamic Analysis of SDA Motion*

To explore the dynamic behaviors of the SDA, including friction effects, an SDOF mass-spring-damper model shown in Fig. 5(a) is proposed. The equation of motion is given as

$$m\ddot{x} + c\dot{x} + \mu F_N \text{sign}(\dot{x}) + kx = F_O^* \text{abs}[\sin(\omega t)]. \tag{26}$$

The variable x represents the displacement of the SDA. The lump-mass m defines the total mass of the SDA array. The coefficient k is the spring constant of the suspended spring. The damper may contain two types of friction: Coulomb friction of coefficient μ and viscous damping of coefficient c. F_N is the normal force between the contact area of the main beam and the insulated layer. In MEMS, the body force, similar to the gravity force, is often much less than the surface traction force, which is also similar to the electrostatic force. So the normal force is simplified to contain only the electrostatic force in the contact area. F_O is the amplitude of the driving force, which is the horizontal component of the electrostatic force along the noncontact part of the main beam, and the force along the bushing is still ignored. The driving voltage is in sinusoidal wave $\sin(\omega t)$ with frequency ω. However, it is noted that the electrostatic force in an SDA is always attractive between contact surfaces. Therefore, the driving force waveform is the same as the absolute of the driving voltage waveform. The friction terms in Eq. (26) may be normalized and rearranged as follows:

$$\frac{c}{m}\dot{x} + \frac{\mu F_N}{m}\text{sign}(\dot{x}) = \text{sign}(\dot{x})^*[\text{gain}^*\text{abs}(\dot{x}) + \text{offset}]. \tag{27}$$

The gain is defined as c/m and the offset is the normalized dry friction force is defined as $\mu F_N/m$. To simplify derivation, both static and dynamic dry friction coefficients are assumed to be μ.

A Simulink™ model is built according to Eqs. (26) and (27), as shown in Fig. 5(b). The function block, called the "Coulomb and Viscous Friction," models the discontinuity at zero velocity and linear gain otherwise. The offset corresponds to the normalized Coulomb friction and the gain corresponds to the normalized viscous friction. As a result, this block is implemented as

$$y = \text{sign}(u) * [\text{gain} * \text{abs}(u) + \text{offset}], \tag{28}$$

where y is the block output and u is the block input. The gain and offset are the normalized block parameters c/m and $\mu F_N/m$, respectively. When the Coulomb friction is ignored, the response subjected to cyclical input $F_{O*}\text{abs}[\sin(\omega t)]$ may be underdamping, critical damping, or overdamping according to whether the discrimination term ($c^2 - 4$ km) is less than, equal to, or larger than zero. These phenomena are classified as a vibration-induced displacement problem,[10,11] which explains in principle the reason why some SDAs do scratch forward but some do not.

When friction is considered, the analysis of displacement response becomes more complex.[15,16] Here Matlab™ and Simulink are used to numerically simulate the dynamic behaviors of SDA.

3 Fabrication and Measurements

A two-mask microelectroplated nickel process is developed to fabricate an Ni SDA array structure. The test structure is composed of four SDAs connected to a suspended spring that is anchored to the contact electrode.

The fabrication process, shown in Fig. 6, is summarized as follows: (a) Starting from a 4-in. RCA-clean (100) wafer, a 6000-Å thick LPCVD silicon nitride is grown in a furnace as the dielectric layer. (b) In the first patterning process: a 2-μm photoresist FH6400 is coated as the sacrificial layer, receives a 90°C soft bake for 10 min, as well as a hydration reaction for 20 min, and then the pattern of bushing and contact electrode by the first mask is created. (c) In the sputtering process, 200-Å-thick Ti and 1500-Å-thick Cu are sequentially sputtered as the adhesive and seed layers, respectively. (d) In the second patterning process, a 5-μm-thick photoresist AZ9260 is coated, then the pattern of the electroplating mold by the second mask is created. (e) In the electroplating nickel process, the Ni test structure is electroplated with a Watt bath with a current density of 10 mA/cm^2 for 10 min to form 2-μm-thick Ni. (f) In the releasing process, acetone is used to remove electroplating mold AZ9260, then the Cu seed layer

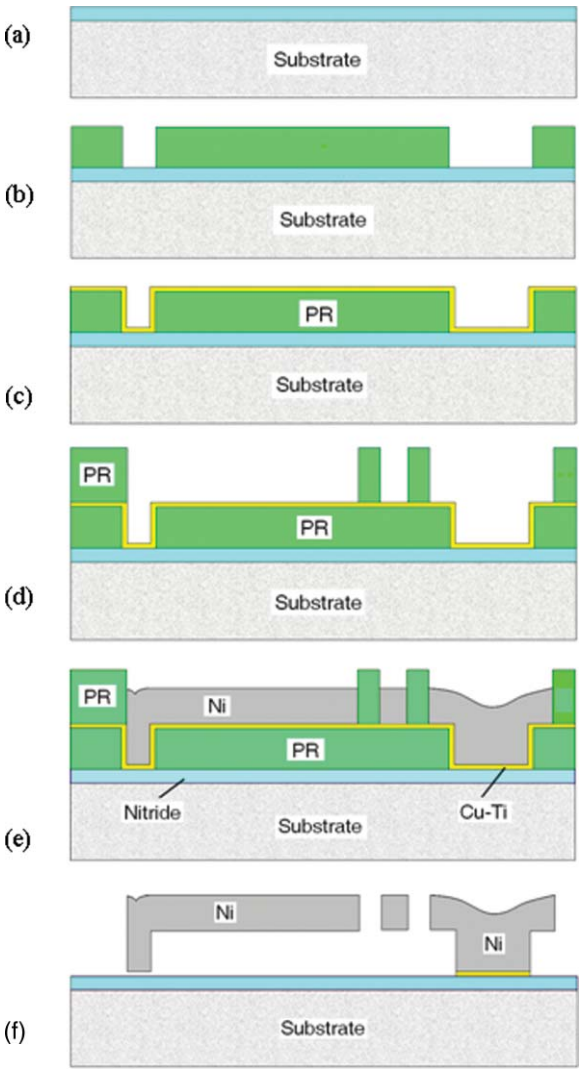

Fig. 6 Fabrication process of the microelectroplated nickel SDA. (a) LPCVD Si_3N_4. (b) Bushing and fixture patterning. (c) Cu/Ti seed layer. (d) Device structure patterning. (e) Nickel electroplating. (f) Releasing.

is removed by soaking in a CR-7T solution for about 20 s. A Ti adhesive layer is then removed by soaking in a buffered oxide etch solution for about 10 s. Then, the FH6400 sacrificial layer is removed by soaking in acetone for 30 min. By immersing in an isopropyl alcohol solution and vibrating about 20 s for releasing, then drying at 60°C, a fully suspended Ni SDA structure can be obtained. A typical fabricated device is shown in Fig. 7. The dimension parameters used in subsequent analyses are measured and listed as follows: number of SDAs per device, $N = 4$; main beam length, $L = 80.8\ \mu$m; main beam width, $W = 65\ \mu$m; thickness, $t = 2.1\ \mu$m; bushing height, $h = 2.2\ \mu$m; support beam length, $L_s = 25.0\ \mu$m; and support beam width, $W_s = 4.0\ \mu$m. Other material properties are adopted from Sharpe et al.,[17] Mazza et al.,[18] and Cho et al.,[19] including Young's modulus, $E = 176$ GPa and shear modulus, $G = 67$ GPa.

The experimental equipment for the loading test includes an optical microscope mounted with a CCD camera on a probe station connected to a PC with image process software, a function generator, and a high-voltage power amplifier. The

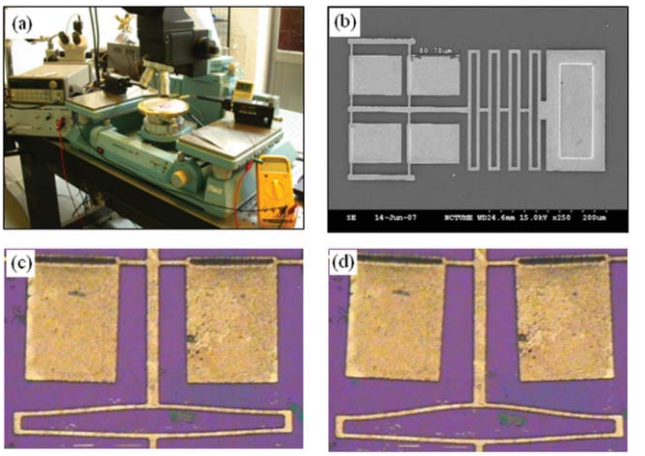

Fig. 7 Typical images of the SDA array. (a) Experimental setup. (b) SEM image of whole released test structure. The width of the SDA main plate is 65 μm and the outer size of each tether spring is 200 μm × 18 μm with a linewidth of 4 μm. (c) Partial image of device at an early stage with small spring deflection. (d) Partial image near the final stage with large spring deflection.

test chip is fixed on the probe station table by vacuum chuck. Two probes are adjusted to touch the contact electrode of the SDA array and the substrate, respectively. The test signal is generated from the function generator and amplified and calibrated by the high-voltage power amplifier to be 40–120 V in sinusoidal waveform of 500 Hz with 10 V increment. The motion of the SDA array is recorded from the CCD camera into the computer and then analyzed by image process software. Typical images of a fabricated device under cyclic load are shown in Fig. 7.

4 Results and Discussions

4.1 *Static Analysis of SDA Deflection*

Numerical codes on MATLAB software are developed to perform the deflection analysis on the proposed static model based on parameters listed in Sec. 3. The noncontact length l_n is calculated from Eq. (16) at each specified input voltage in a postpriming state. The results are plotted in Fig. 8. The

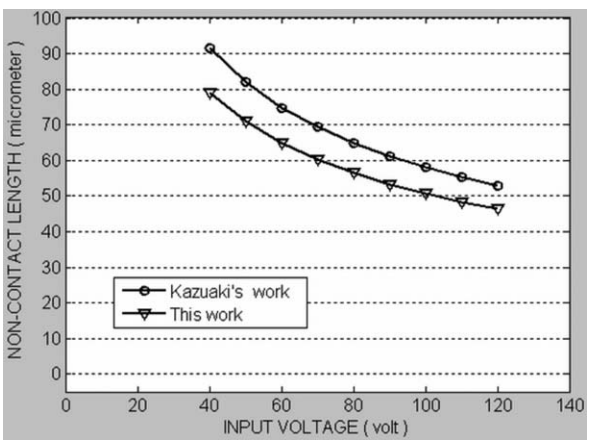

Fig. 8 Noncontact length of SDA against input voltage. Noncontact length means the minimum plate length to keep the SDA priming for given inputs. Kazuaki's work is calculated from the equation proposed in Ref. 7.

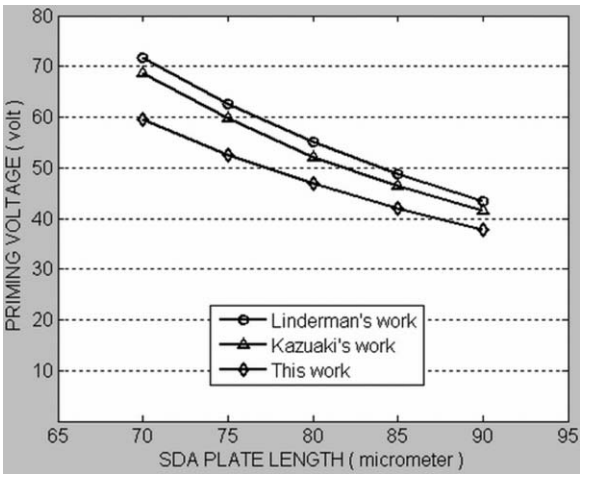

Fig. 9 Simulated results on priming voltage. All models show that the shorter plate has a higher priming voltage. Linderman's work is calculated from the equation in Ref. 5.

priming voltages are calculated from Eq. (17) and plotted in Fig. 9. The noncontact length decreases fast at the beginning of the postpriming region because a longer beam is more flexible. The slope of the noncontact length curve becomes flatter near 120 V, indicating that the electrostatic force is struggling to deform the main beam further. The contact length l_c, equal to $(L - l_n)$, should be long enough to provide a sufficient fixing force to hold the main beam contact part still, although it should be short enough to discharge quickly. The simulated static step sizes, with and without the curvature shortening effect and from Kazuaki's[7] model, are shown in Fig. 10. The proposed model with the curvature shortening effect is found to provide the smallest step size.

The calculated total travel distances by Eq. (25) during 1500 input pulses are plotted in Fig. 11 for five different input voltages, from 80 to 120 V. The experimental results after 1500 pulses are also shown in Fig. 11. The SDA array moves rapidly at the beginning. Then, the motion tends to slow down with an increase in spring force until the SDA array can no longer pull the spring. It will reach a stable state faster at lower input voltages because of the smaller output force.

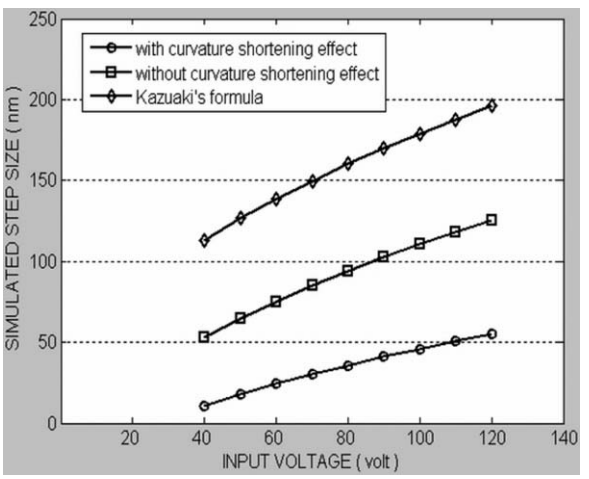

Fig. 10 Simulated static step size by different models. This work predicts the most conservative step size.

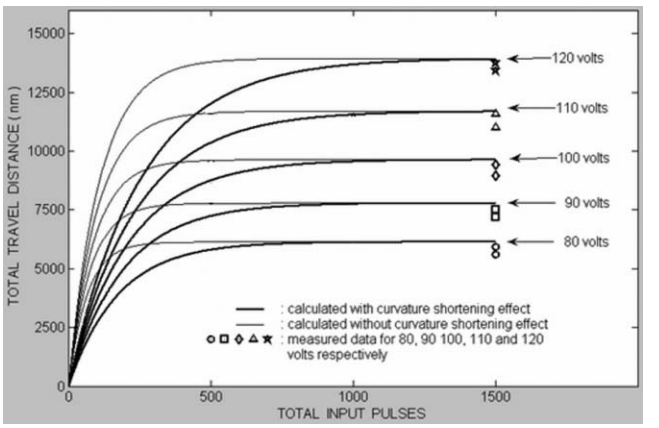

Fig. 11 Measured and simulated total travel distances in 1500 input pulses for voltages from 80 to 120 V. Simulated results are based on Eqs. (24) and (25), and friction is not considered in these simulations.

The measured travel distances are smaller than the simulated results, where the maximum deviation between the measured and the calculated total travel distance is around 10%. From Eq. (20), the maximum bending moments M_m along the main beam at different input voltages can be calculated. From Eq. (21), the maximum bending stresses σ_m are calculated to be from 169 to 495 MPa, as shown in Fig. 12, for input voltage from 40 to 120 V, respectively. However, the displacements of an SDA cannot be steadily measured for input voltage below 80 V. It is believed that the contact length is not long enough to provide sufficient friction force for the SDA array to steadily step forward for voltages below 80 V.

4.2 *Dynamic Analysis of SDA Motion*

From the standard test specimen in this work, the total device mass m and spring constant can be calculated as 4.87×10^{-10} kg and 2.19 μN/μm, respectively, according to the material properties and measured device dimensions. The corresponding normalized spring constant k/m of the fabricated device is then 4.5×10^{9}. Two other normalized spring constants, 3.6×10^{9} and 5.63×10^{9}, are also used in simulations to show the effect of spring-constant variation on device responses.

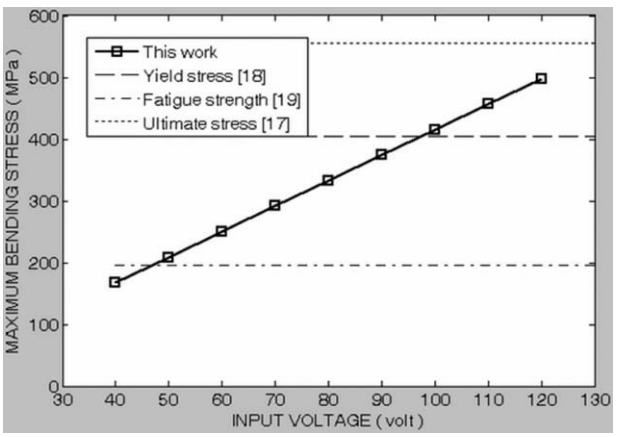

Fig. 12 Simulated maximum bending stress. Device can survive 1×10^{6} cycles with stress less than fatigue strength. Device may have short life cycles with stress around yielding stress. Stress at ultimate stress makes the device immediately fail.

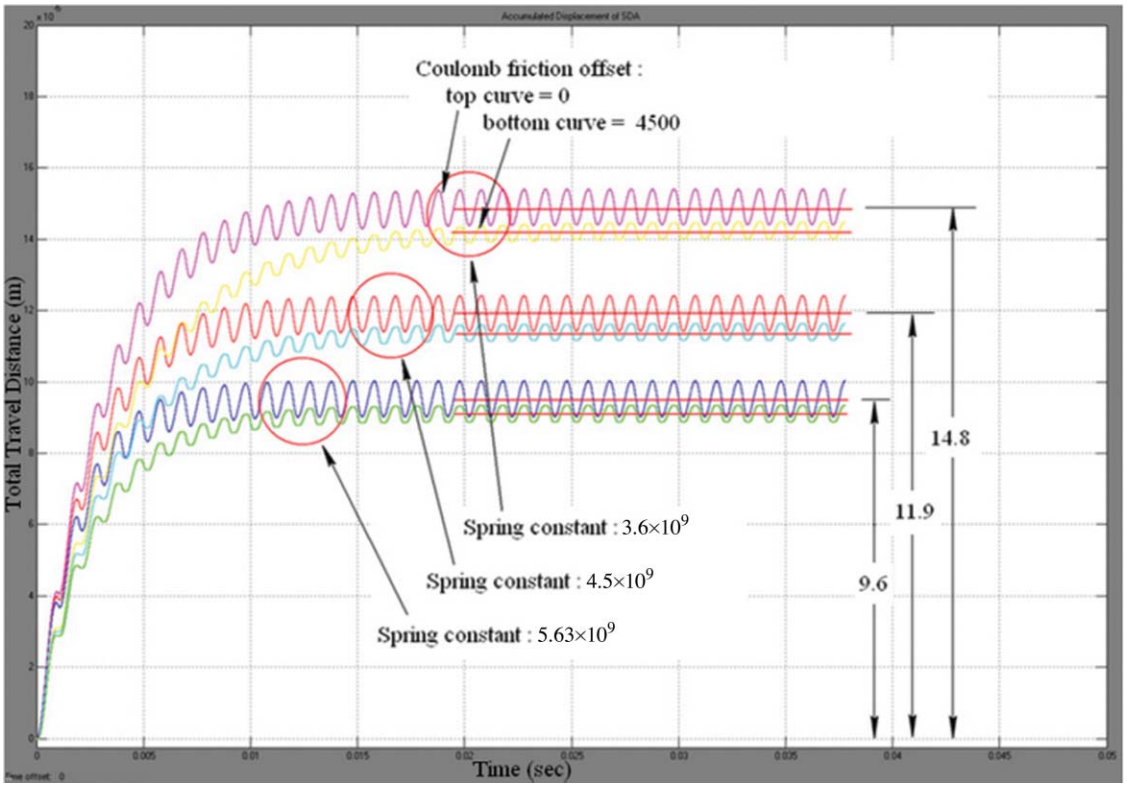

Fig. 13 Effect of spring constant on travel distance. Parameters: 120 V, $m = 4.87\times10^{-10}$ kg; viscous friction c/m is fixed at 1.12×10^{7}, $k/m = [3.6\times10^{9}, 4.5\times10^{9}, 5.63\times10^{9}]$, Coulomb friction $\mu/m = [0, 4500]$.

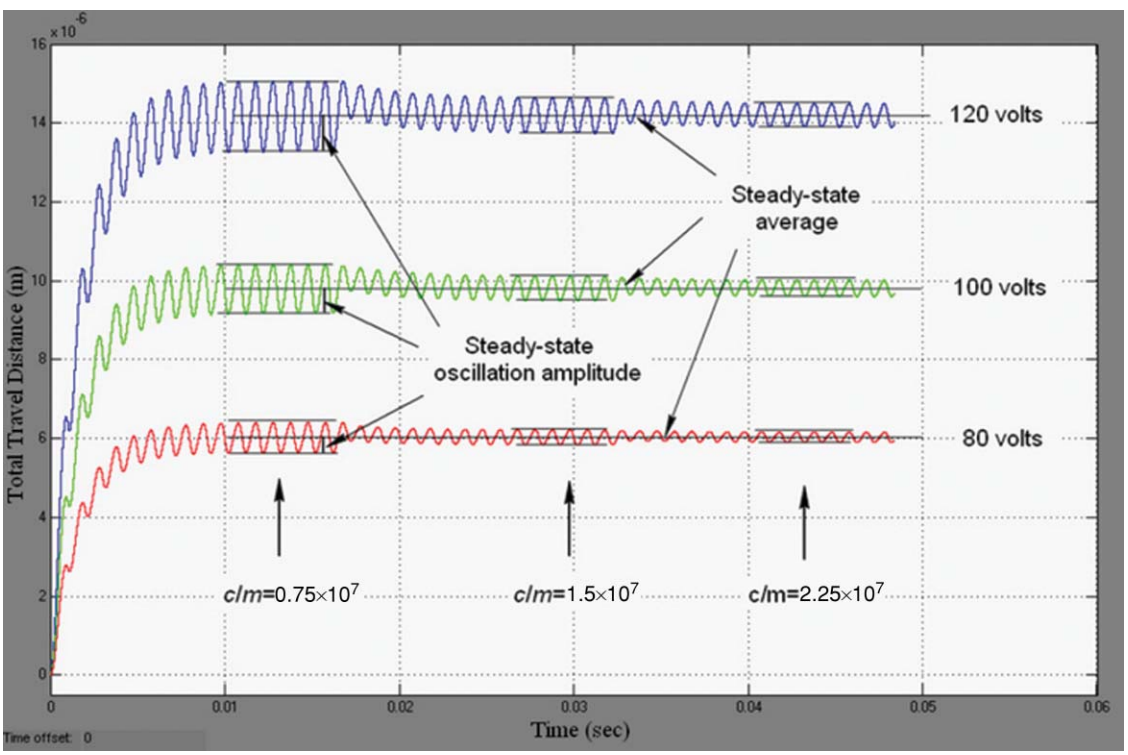

Fig. 14 Effect of viscous damping on travel distance. $c/m = [0.75, 1.5, 2.25]\times10^{7}$, k/m is fixed at 4.5×10^{9}, μ/m is set as zero, at 3140 rad/s, $m = 4.87\times10^{-10}$ kg.

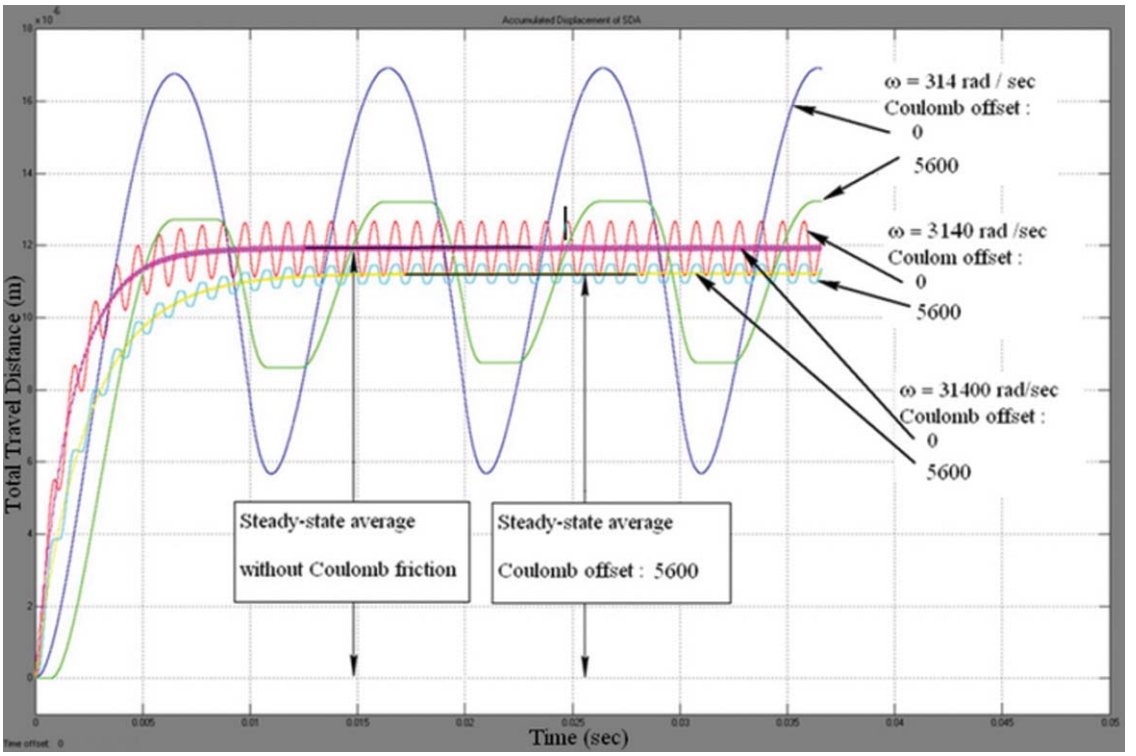

Fig. 15 Driving frequency effect on travel distance. Parameters: 120 V, $k/m = 4.5\times10^{9}$, $c/m = 0.75\times10^{7}$, μ/m = [0, 5600], driving frequency = [314 3140 31400] (rad/sec), $m = 4.87\times10^{-10}$ kg.

The scale ratio for the other two spring constants is set to be 1.25, i.e., 5.63/4.5 = 4.5/3.6 = 1.25. The undamped natural frequency ω_n of the equivalent SDOF system is about 67 000 Hz, much higher than the driving frequency of 500 Hz; therefore, the system can be classified as a stiff system.[20] Since the viscous friction coefficient and the Coulomb friction coefficient are not yet known exactly in the current device or from previous literature about the SDA, various parameter sets are simulated to find out the better-matched parameter set with experimental results.

Figure 13 shows the simulated total travel distances of the SDA at three different spring constants. Each spring constant is accompanied by two different Coulomb friction values, zero and 4500. The average steady-state displacement of each curve is shown to decrease with an increase in spring constant. The Coulomb friction is found to reduce both the average and the amplitude of displacement due to the stick-slip effect.

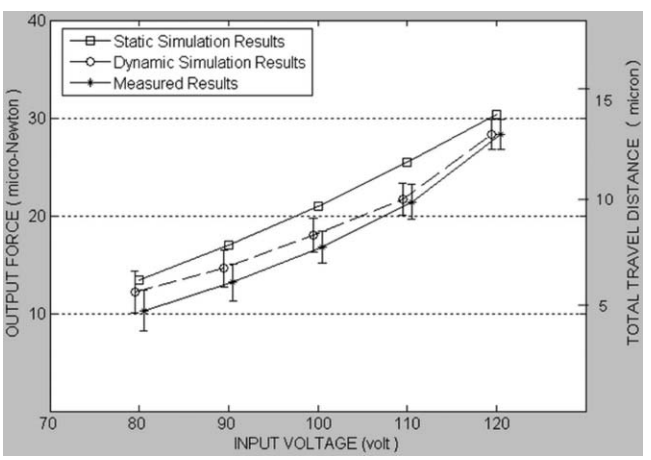

Fig. 16 Output forces and total travel distances from static model, dynamic model, and experimental data.

To learn the effects of viscous friction, the simulated total travel distances for three different viscous friction ratios are shown in Fig. 14. For the specific input voltage, the average displacement is nearly the same for the three different viscous friction ratios. The oscillation amplitude at steady state is more evident as the c/m ratio decreases. The simulated total travel distances at 120 V with different driving frequencies are shown in Fig. 15. For a specific Coulomb offset, the averaged displacement at steady state is almost the same, but the oscillating amplitude is quite different. The oscillating amplitude is found to decrease with an increase in driving frequency. This phenomenon was also discussed in Thomsen[21] for nonlinear oscillation. Based on its concept, the SDA may be viewed as a low-pass filter that will pass the low-frequency component and attenuate the component amplitude at a higher frequency. Therefore, it is better to drive the SDA at a higher frequency to reduce oscillations.

As mentioned earlier, the Coulomb offset and the viscous friction coefficient are both not exactly known in the experiment. Therefore, a manual matching process between simulations and experimental results is performed to identify a closer parameter set on viscous friction and Coulomb friction. Finally, a better matched set is found where the normalized viscous friction c/m ratio is 0.40×10^{6} and the Coulomb friction offset ratio μ/m is 15 000. Due to the limitation of our facilities, our image capture system cannot capture

the oscillating waveform in nanometer resolution. However, Fig. 16 compares the experimental results with simulations from static and dynamic models, including output force and total travel distance. It is shown that simulations from the dynamic model are closer to the measured total travel distance and the output force than to the static model, in general. This indicates that difference between simulations and experimental data due to energy dissipation can be reduced by including the friction effect in the dynamic model.

5 Conclusion

Static and dynamic models of a rectangular SDA are proposed here. The improved static model provides a more systematic approach to simulate many key characteristics that were not fully presented in previous literatures. The dynamic model is driven by the output force derived from the static model. It considers the SDA device as an SDOF mass-spring-damper system to evaluate the dynamic behaviors at steady state. The vibration-induced displacement of the SDA subjected to various factors has been simulated and discussed. A parameter set on friction to match with experimental results is suggested for the fabricated microelectroplated nickel SDA device. By properly considering the friction effect, dynamic simulations are shown to be closer to the experimental data than to static simulations because of the included energy dissipation. The proposed models have the potential to be further modified to analyze SDAs other than those of a rectangular shape.

Acknowledgments

This work was supported by the National Science Council of the Republic of China under Grant No. NSC922212E009035. We appreciate the technical support provided by the staff of the Nano Facility Center of NCTU.

References

1. T. Akiyama and K. Shono, "Controlled stepwise motion in polysilicon microstructures," *J. Microelectromech. Syst.* **2**(3), 106–110 (1993).
2. T. Akiyama, D. Collard, and H. Fujita, "Scratch drive actuator with mechanical links for self-assembly of three-dimensional MEMS," *J. Microelectromech. Syst.* **6**(1), 10–17 (1997).
3. L. Fan, M. C. Wu, K. Choquette, and M. H. Crawford, "Self-assembled micro-XYZ stages for optical scanning and alignment," *Transducers*, pp. 319–322, IEEE, Chicago, IL (1997).
4. E. Quévy, L. Buchaillot, and D. Collard, "3-D self-assembling and actuation of electrostatic microstructures," *IEEE Trans. Electron Devices* **48**(8), 1833–1839 (2001).
5. R. J. Linderman and V. M. Bright, "Nanometer precision positioning robots utilizing optimized scratch drive actuators," *Sens. Actuators, A* **91**, 292–300 (2001).
6. Y. Kanamori, Y. Aoki, M. Sasaki, H. Hosoya, A. Wada, and K. Hane, "Fiber-optical switch using cam-micromotor driven by scratch drive actuators," *J. Micromech. Microeng.* **15**, 118–123 (2005).
7. H. Kazuaki, A. Torii, and A. Ueda, "An analysis of the elastic deformation of an electrostatic microactuator," *IEEJ Trans. Sens. Micromachines* **118-E**(3), 205–211 (1998).
8. B. R. Donald, C. G. Levey, C. D. McGray, D. Rus, and M. Sinclair, "Power delivery and locomotion of untethered microactuators," *J. Microelectromech. Syst.* **12**(6), 947–959 (2003).
9. L. Li, J. G. Brown, and D. Uttamchandani, "Study of scratch drive actuator force characteristics," *J. Micromech. Microeng.* **12**, 736–741 (2002).
10. E. C. Miranda and J. J. Thomsen, "Vibration induced sliding: theory and experiment for a beam with a spring-loaded mass," *Nonlinear Dyn.* **16**, 167–186 (1998).
11. A. Fidlin and J. J. Thomsen, "Predicting vibration-induced displacement for a resonant friction slider," *Eur. J. Mech. A/Solids* **20**, 155–166 (2001).
12. J. M. Gere and S. Timoshenko, "Shear forces and bending moments," Chap. 4 in *Mechanics of Materials*, PWSKENT, Boston, MA (1990).
13. K. E. Petersen, "Dynamic micromechanics on silicon techniques and devices," *IEEE Trans. Electron Devices* **25**, 1241–1250 (1978).
14. S. Timoshenko and J. N. Goodier, "Torsion of prismatic bars," Chap. 11 in *Theory of Elasticity*, Maple Press, York, PA (1951).
15. S. Andersson, A. Soderberg, and S. Bjorklud, "Friction models for sliding dry, boundary and lubricated contacts," *Tribol. Int.* **40**, 580–587 (2007).
16. A. Fidlin, "Oscillations in systems with dry friction," Chap. 2 in *Nonlinear Oscillations in Mechanical Engineering*, Springer-Verlag, Berlin (2006).
17. W. N. Sharpe, Jr., D. Lavan, and R. Edwards, "Mechanical properties of LIGA deposited nickel for MEMS," *Transducers*, pp. 607–611, IEEE, Chicago, IL (1997).
18. E. Mazza, S. Abel, and J. Dual, "Experimental determination of mechanical properties of Ni and Ni-Fe microbars," *Microsyst. Technol* **2**, 197–202 (1996).
19. H. S. Cho, K. J. Hemker, K. Lian, J. Goettert, and G. Dirras, "Measured mechanical properties of LIGA Ni structures," *Sens. Actuators, A* **103**(1–2), 59–63 (2003).
20. L. Meirovitch, "Single-degree-of-freedom systems," Chap. 3 in *Principles and Techniques of Vibrations*, Prentice Hall, Englewood Cliffs, NJ (1996).
21. J. J. Thomsen, "Some general effects of strong high-frequency excitation: stiffening, biasing and smoothening," *J. Sound Vib.* **253**(4), 807–831 (2002).

Shawn Chen received his PhD degree in mechanical engineering from the National Chiao Tung University, Taiwan, in 2010. He is an associate professor now in the mechanical engineering department of National Chinyi University of Technology, Taiwan. His current interest focuses on the design of microtransducers.

Chiawei Chang received his MS degree in mechanical engineering from the University of National Chiao Tung University, Taiwan, in 2007.

Wensyang Hsu received his MS and PhD degrees in mechanical engineering from the University of California, Berkeley, in 1990 and 1992, respectively. He is a professor in the mechanical engineering department of National Chiao Tung University, Taiwan. His current interests include design and fabrication of microactuators and sensors.